# Enhancement of momentum transfer of bubble swarms using an ejector with water injection

Hyunduk Seo[1], Aliyu M. Aliyu[2], Kyung Chun Kim* [1]

[1]School of Mechanical Engineering, Pusan National University, 609-735, Busan, Republic of Korea

[2] Gas Turbine and Transmissions Research Centre, Faculty of Engineering, University of Nottingham, NG7 2RD, United Kingdom

* Corresponding author: Kyung Chun Kim, kckim@pusan.ac.kr

## Highlights

1. Bubble swarms characteristics generated from ejectors are experimentally investigated
2. Digital image processing is carried out to obtain statistical data of bubble swarm
3. Momentum transfer is demonstrated by a buoyancy experiment with a spherical model
4. Uniform bubble swarm is realized by the proposed ejector with water injection

## Abstract

This paper presents the application and a comparative study of two ejector configurations to enhance the momentum transfer of submerged bubble swarms generated in a water tank. High-speed photography was used to measure the bubble rise velocity profiles and bubble size distribution from captured images. The volumetric flowrate of air was varied from 2 to 15 L/min, and water was supplied at 70 L/min for the case with water injection. Three different cases were selected to conduct bubble swarm visualization: one with a plain nozzle, one with an air-driven ejector, and one with a water-driven ejector. Buoyancy experiments were also carried out to characterize momentum transfer capability. The plain nozzle and air-driven ejector cases make ergodically large bubbles. However, in the case with water injection, small bubbles were generated through the suction and mixing chamber inside the ejector, and evenly sized broken-up bubbles came out. Due to the differences in bubble generating mechanisms, there were specific differences in the bubble characteristics. The case with water injection showed significant buoyancy performance for the spherical model compared to the other cases.

**Keywords:**

Bubble swarm, ejector, momentum transfer, bubble break-up

## 1. Introduction

Bubble-driven flows are used in various industrial and environmental applications, such as wastewater treatment, bubble column reactors, pharmaceutical and food processing, and lake restoration processes [1-3]. Generally, the goal is to enhance the transfer of mass, momentum, and energy between the phases. To achieve this, interaction should be increased between the phases by changing bubble dispersion characteristics. Particularly, finely distributed bubbles are the most important flow characteristic that contribute to the efficiency of the mixing process [4, 5]. However, bubbles can grow and agglomerate near inlet orifices until upward forces overwhelm the surface tension force, hydrodynamic force, and other forces. Because of this, fine bubble distributors have been developed over the years.

Researchers have tried to enhance and control chemical reactions by using spargers, which consist of a bundle of pipes with tiny holes [6-8]. The holes generate small bubbles and are sparsely positioned on plates or pipes to prevent departing bubbles from coalescing near each other. However, “weeping” can result in undesirable residence of the bubbles on the sparger, which should be considered in the design process. To avoid weep conditions, the critical weep velocity should be achieved at each hole. Furthermore, there is a considerable pressure drop in the sparger, which should be improved by shape optimization or other techniques [7]. Nevertheless, spargers are often used because of their low installation cost.

Ejectors are often used to generate even smaller micro-bubbles in addition to milli-bubbles [1]. Ejectors are widely used to transport a secondary fluid to another place with driving force from a primary fluid. Because of the pressure difference between the suction chamber and secondary flow, the secondary fluid can be entrained in the main flow in the form of small droplets or bubbles [9]. Cramers et al. [10] and Dutta and Raghavan [11] showed that a liquid jet ejector can enhance the mass transfer characteristics of loop reactors. Fujiwara et al. [12]

investigated an upward venturi type micro bubble generator and it showed remarkable bubble generation performance in comparison with needle type generators. Also, these studies reported that small bubble sizes improved the overall gas hold-up characteristics [10-12]. Bubble size distributions inside ejectors have also been reported with various volume fractions and average bubble size generated from an ejector with gas deficit conditions ($\sim \alpha = 0.4$) [13, 14]. Previous researches are summarized in the Table 1 with their experimental conditions, measurement techniques, and remarkable achievements. From the literature review, ejectors showed more potential to generate bubble swarms that consist of finely dispersed bubbles than other methods due to the bubble breakup characteristics caused by the pressure loss in the convergent region. However, the characteristics of bubbles generated from ejectors have not been widely reported. This study experimentally investigates characteristics of the ejector driven bubble swarm by measuring bubble equivalent diameter, bubble size distribution, representative bubble velocity and bubble aspect ratio. The objective of this study is introduce an effective bubble generating system which can replace conventional bubble generating system such as horizontal tubes in gas-fluidized bed [15, 16] or spargers in bubble column reactors [6-8]. There is still necessity on effective and economical design of mixing and reaction system [16, 17] and it can be realized by the proposed method due to enhanced bubble characteristics such as (1) uniformly sized bubbles which is essential parameters to control reaction in the system (2) wider diverge angle with increased gas hold-up and wide coverage area for installation of cost reducing system (3) enhanced interaction and mixing characteristics between bubbly flow and the particle to improve reaction performance. Furthermore, improved bubble characteristics can find applications in various energy fields such as (1) biomass gasification (with relatively low working temperature) using bubbling fluidized bed reactors to promote mixing characteristics between fluid, gas, and particles [18] (2) desalination systems by replacing conventional water sprays with bubble columns [19, 20]. The performance of applying the ejector with water injection should be analyzed quantitatively because operating conditions in each application can have significant effect on energy consumption and efficiency of system [17].

To investigate bubble characteristics, previous researchers have used various methods such as bubble imaging for bubble shapes and bubble trajectories, measurement with intrusive probes, particle images of continuous field to obtain velocity field around bubbles, and so on. In this study, we used high-speed photography to obtain bubble characteristics including equivalent bubble diameter, aspect ratio of bubble and averaged bubble velocity of each case. In cases of high gas flux, bubble swarm cannot be completely resolved by high-speed photography due to massive bubble overlap. To avoid optical problems, advanced high resolution and high frequency technologies such as X-ray can be used. Because X-ray have low applicability for various problems occurring in industry and environment due to expense and hard for installation, they cannot be practically utilized in these days.

## 2. Experimental setup and image acquisition

### 2.1. Experimental setup

A diagram of the experimental setup is shown in Figure 1 (a). Experiments were conducted in the 1-$m^3$ water tank filled with filtered tap water up to 90%. The tank was washed out after each case and re-filled. Most experiments we saw in literature were conducted with tap water or purified water and comparison between literature studies and results from the present study will be discussed in Chapter 4. A plain acrylic nozzle is located at the bottom of the tank. To compare the effectiveness of the ejectors, three different cases of bubble generation were conducted: one with a plain nozzle, one with an air-driven ejector, and one with an ejector with water injection.

The plain nozzle is an acrylic pipe with a 5-mm inner diameter and 8-mm outer diameter. The ejector was machined from acrylic, and then the inside was polished with a fine abrasive. The draft and a picture of the ejector are shown in Figure 1. The overall ejector geometry is similar to the half-scaled center-driven ejector fabricated by Kim et al. [21]. To promote entrainment of water, (1) the gap between the exterior of the nozzle and the suction chamber is decreased (2) the nozzle exit is located near the contraction part between the suction chamber and the mixing chamber. Two ejectors with the same geometry were fabricated but the case with water injection includes an additional part for water injection as shown in Figure 1 (b) and (c). The exit of the nozzle and ejector were 140 mm and 244 mm above the bottom of the tank, respectively.

In the bubble generation with water injection case, water is supplied at 70 L/min into the suction chamber from an immersed water pump. Compressed air is supplied to nozzle through a pressure regulator and rotameter connected in series. The chosen rotameter (Dwyer RMA-22) is operated at 2–15 L/min with 4% error of the full-scale range (2 – 25 L/min). Bubble swarms generated from the nozzle and ejectors were recorded by high-speed photography. Liu et al. and Ravelet et al. [22, 23] recorded bubble images using two perpendicularly positioned cameras or mirror to measure the diameter and the aspect ratio of single bubble. In the present study, a high-speed

CMOS camera (Photron SA1.1) is used to record bubble images due to difficulty of recoding bubbles in the bubble swarms with two or more cameras. The high-speed CMOS camera and the field of view (FOV), and the light source (200 W LED Lamp) aligned straight are shown in Figure 1 (a). Light passing through a light diffuser is used to illuminate the bubble flows, and the edges of bubbles are projected as shadows.

### 2.2. Experimental procedure

The three different cases (a plain nozzle, an air-driven ejector, and an ejector with water injection) were arranged with six different air flowrate cases (2, 3, 5, 7, 10, and 15 L/min corresponding to air velocities at the nozzle $u_g$ of 1.70, 2.55, 4.24, 5.94, 8.49, and 12.7 m/s). Before the implementation of each case, the needle valve of the rotameter was opened, and then the supplied pressure and volumetric flow rates of air were adjusted until the fluctuation of the floats became steady. A total 18 cases of experiments were carried out, and bubble swarms were recorded for 5 s.

Bubble images were recorded at 1000 frames per second with a shutter speed of 1/2000 seconds. Furthermore, an 85-mm f/2.8D Nikkor lens was used. Therefore, the high-speed photography shows a narrow depth of focus, and bubble motions are clearly captured in focus. The edges of bubbles that are out of focus are distinguished from the other parts. Figure 2 shows a snapshot of bubble swarms in each case. The recorded images have a magnification of 0.2 mm/pixel and resolution of 1024 × 1024 pixels, which corresponds to the size of the FOV (about 205 mm × 205 mm).

## 3. Data reduction and analysis

### 3.1. Digital image processing

Before analyzing the characteristics of bubble swarms, the recorded high-speed photographs (uncompressed 16-bit TIFF format) have to be converted into binary images to distinguish each phase. Shen et al. and Busciglio [24, 25] captured RGB images from a fluidized bed and identified the phases by assigning a threshold value. The bubbles and the continuous phase in the captured images have different intensities, so proper universal threshold values can be used to separate each phase by digital image processing.

In the case of bubbles in water, however, the light intensity inside of the bubbles is similar to that of the background. Sadr-Kazemi and Cilliers and Lau et al. [26, 27] developed an image analysis method using a watershed transformation function to separate overlapped bubble images into individual bubbles. Lau et al. [27] validated their "water-shedding technique" with synthetic bubble images and bubble images captured from pseudo-2D bubble column case. Without water-shedding technique, overlapped bubbles are recognized as individual bubble and it was discarded by shape factor. Water-shedding technique resulted in reduced number of discarded bubbles as much as 3 times smaller than without water-shedding technique. But, two different results showed similar peaks of PDF regarding bubble size. Additionally, each image processing technique has different features as follows: (1) the image processing with water-shedding technique showed overestimated bubble size distribution in poly-dispersed bubbles and underestimated bubble size in monodispersed bubbles but the peak of PDF regarding bubble size was remained; (2) the image processing without water-shedding technique showed PDF with peak concentrated profile regarding bubbles size and there are so many discarded bubbles that it may be needed to collect huge amount of sample images. For more reliable bubble size measurement in complex flow with large bubbles, Ziegenhein et al. and Besagni and Inzoli [28, 29] dealt bubble by using hand picking to identify bubble's size. As a result, Ziegenhein et al. [29] reported that this technique showed fairly good error as 15% underestimation in their experiment with air-lift reactor, and Besagni and Inzoli [28] report approximately 300 bubbles with hand-picking can present reliable bubble size distribution in their experiment with bubble column with a sparger. Xu et al. and Aliyu et al. [30-33] used a series of image processing steps consisting of (1) background subtraction (2) thresholding and filtering, (3) edge detection, (4) edge dilation, (5) filing holes and (6) edge erosion process to get bubble boundary. Aliyu et al. [31] reported that mean diameter of bubble obtained from this technique showed good agreement with literatures. But, it is hard to neglect all out-of-focus bubbles by thresholding process. Furthermore, overlapped bubbles also can be recognized as an individual bubble. In this study, to reduce computational resources, and to neglect overlapped bubbles, a series of image processing steps consisting of (1) Gaussian filtering, (2) edge detecting, (3) edge dilation, (4) filling holes, (5) edge erosion and (6) bubble neglecting using shape factors which is realized by comparison between eroded images and subtracted filtered image (subtracted from raw images). The step for neglecting unfocused or overlapped bubbles utilizes the following feature of recorded bubble edge: (1) unfocused bubbles have blurred outline with lower grayscale intensity gradients (2) overlapped bubbles have relatively long outlines than their volume. From these features, we can distinguish whether the bubble is unfocused or overlapped by counting the number of pixels on the bubble's outline, after subtracting a gaussian blurred image from a raw image: (1) an unfocused bubble which has an already blurred outline will be almost removed and edge detection on subtracted images will yield small number of pixels on bubble outline (2) overlapped bubble will yield too many number of pixels. Detailed strategy on the bubble neglecting process is described in the next paragraph. For edge detecting as shown in Figure 3 (b), the Prewitt method was adopted to converse grayscale image to binary lined image [34]. For Prewitt method, global threshold value considering grayscale gradient all over the image is obtained by trial and errors. Unfortunately, complete removal of unfocused bubbles is difficult to achieve in this process due to small parts of focused bubbles are also affected by stiff threshold value. The Prewitt method has the benefit of computational speed due to simple horizontal and vertical mask but, the method is weak in diagonal edge detection. As shown in equation 1, Prewitt edge detection uses two different masks which have horizontally and vertically arranged elements, respectively.

$$\boldsymbol{K_h} = \begin{bmatrix} \mathbf{1} & \mathbf{0} & \mathbf{-1} \\ \mathbf{1} & \mathbf{0} & \mathbf{-1} \\ \mathbf{1} & \mathbf{0} & \mathbf{-1} \end{bmatrix}, \boldsymbol{K_v} = \begin{bmatrix} \mathbf{-1} & \mathbf{-1} & \mathbf{-1} \\ \mathbf{0} & \mathbf{0} & \mathbf{0} \\ \mathbf{1} & \mathbf{1} & \mathbf{1} \end{bmatrix} \qquad (1)$$

For horizontal edge detection, a simple computing process which calculates grayscale gradient along horizontal direction can be expressed as equation 2:

$$\boldsymbol{I_h} = \begin{bmatrix} \boldsymbol{b_{11}} & \boldsymbol{b_{12}} & \boldsymbol{b_{13}} & \cdots \\ \boldsymbol{b_{21}} & \boldsymbol{b_{22}} & \boldsymbol{b_{23}} & \cdots \\ \boldsymbol{b_{31}} & \boldsymbol{b_{32}} & \boldsymbol{b_{33}} & \cdots \\ \cdots & \cdots & \cdots & \cdots \end{bmatrix} = \boldsymbol{I_0} * \boldsymbol{K_h} \qquad (2)$$

$$\textbf{where, } \boldsymbol{I_0} = \begin{bmatrix} \boldsymbol{a_{11}} & \boldsymbol{a_{12}} & \boldsymbol{a_{13}} & \cdots \\ \boldsymbol{a_{21}} & \boldsymbol{a_{22}} & \boldsymbol{a_{23}} & \cdots \\ \boldsymbol{a_{31}} & \boldsymbol{a_{32}} & \boldsymbol{a_{33}} & \cdots \\ \cdots & \cdots & \cdots & \cdots \end{bmatrix}, \boldsymbol{b_{22}} = \boldsymbol{a_{11}} + \boldsymbol{a_{21}} + \boldsymbol{a_{31}} - \boldsymbol{a_{13}} - \boldsymbol{a_{23}} - \boldsymbol{a_{33}}$$

Combination of horizontal and vertical computing process and proper threshold values can be used for edge detecting. So, detected edge of bubble is not completely closed and there could be spaces between detected edges. To complement diagonal detection, there is need to conduct an edge dilation process which expands edges in four directions as shown in Figure 3 (c). Figure 3 (d) shows bubble images with filled holes. Bubble filling process following edge dilation is implemented by replacing all pixels within the completed bubble boundary with unit values. As shown in Figure 3 (e), enlarged bubble boundaries undergo edge eroding process to complement edge dilation process. This process recovers bubble boundaries and each bubble will have the same size with those in the raw image.

Since unfocused bubbles in the raw image seem blurry, unfocused bubbles can be easily separated by subtracting the Gaussian blurred image of Figure 3 (f) from the raw image of Figure 3 (a). Figure 3 (g) shows that unfocused bubble edges in raw image become fainter. Threshold value obtained from Otsu's method is used to binarize the subtracted image and it is overlapped with eroded image as Figure 3 (h). By assuming that the bubbles are absolutely spherical in shape, the length of a detected edge (perimeter) for each bubble should follow the equations:

$$\boldsymbol{p_{i,sphere}} = \boldsymbol{\pi}\, \boldsymbol{d_{b,\mathrm{eq},\mathrm{i}}} = \sqrt{\boldsymbol{4\pi A_{b,\mathrm{i}}}} \qquad (3)$$

$$\boldsymbol{A_{b,\mathrm{i}}} = \iint \mathbf{b_i}(\mathbf{x,y})\, \boldsymbol{dxdy} = \sum \mathbf{b_i}(\boldsymbol{x},\mathbf{y}) \qquad (4)$$

where $p_{i,sphere}$ is the perimeter of the $i$-th bubble, $d_{b,eq,i}$ the is equivalent diameter of $i$-th bubble, $A_{b,i}$ is the area of the $i$-th bubble, and $b_i(x,y)$ is the position of $i$-th bubble in pixelized coordinates. Size of each bubble is calculated from labelled bubble image as shown in Figure 4. However, the actual perimeter detected using digital image processing can vary due to bubble overlap and shape distortion resulting from drag forces exerted on the bubbles and interactions between the bubbles [35]. To distinguish whether bubble is whole individual bubble, the following inequality is proposed:

$$\boldsymbol{s_1\, p_{i,sphere}} \leq \mathbf{p_i} \leq \boldsymbol{s_2\, p_{i,sphere}} \qquad (5)$$

where $\boldsymbol{s_1}$ and $\boldsymbol{s_2}$ are bubble shape factors to limit the detected bubble outlines in accordance with the bubble area. The first shape factor $\mathbf{s_1}$ is criterion to discard unfocused bubbles. As shown in Figure 3 (a), there are unfocused bubbles out of yellow and red circles. By subtracting the raw image from the image with Gaussian filtering, the image of Figure 3 (g) is obtained. In subtracted image, bubbles are expressed with strong or weak intensity of lines according to whether each bubble is focused or not. By using a threshold value, only pixels with strong intensities remain as red dots, and focused bubbles' outline is almost completely filled with red dots as shown in Figure 3 (g). However, unfocused bubbles' outline cannot be filled with red dots because the intensities of many blurred outline pixels were subtracted and thresholded. The first shape factor $s_1$ is used as a bottom limitation to neglect unfocused bubbles based on how the bubble's outline is clear. If $s_1$ is too low, even unfocused bubbles can be recognized as a whole individual bubble. On the contrary, if $s_1$ is too high, (near 1.0) even focused bubble cannot be recognized because reflection and refraction on the edge of bubble result in loss of bubble outline (glared bubble edge cannot be detected by gradient based edge detection algorithm). The second shape factor $s_2$ is criterion to discard overlapped bubbles. Lau et al. [27] referred this factor as "roundness" to identify whether the bubble is spherical or not. As shown in Figure 3 (h), there are too many red dots are resident in the bubble inside red circle. As a result, in Figure 3 (i) and (j), overlapped bubbles are discarded by the value of $s_2$. In this context, $s_2$ should be considered as not only a factor to discard overlapped bubbles but also a limitation of distortion (elliptical or irregular) of bubbles. If $s_2$ is too high, overlapped bubbles can be recognized. On the contrary, if $s_2$ is too low (near 1.0) elliptical or distorted but not overlapped bubbles cannot be recognized. In this study, $s_1$ and $s_2$ showed similar performance within the range of 0.7 ~ 0.9 and 1.4 ~ 1.5, respectively (in this study, 0.7 and 1.5 are used). Using these factors, the image processing algorithm has the chance to select a whole individual bubble and the algorithm can reduce the error resulting from previous automatic algorithms [27, 31]. Furthermore, this algorithm needs a lot of samples to collect sufficient number of whole individual bubbles from images. Therefore, 5000 image samples were used to collect more than hundreds of thousands of bubbles. However, still there are more possibility in error with automatic algorithm used in this study than algorithms aided by manual hand-picking process.

## 3.2. **Bubble rise velocity profiles**

The representative bubble velocity was extracted from binarized bubble image which is obtained after edge eroding process. The reason to use not neglected image but edge eroded image is that bubbles motion is so complex that, bubbles can be focused (and be recognized by the algorithm) but can also be unfocused or overlapped (hence be neglected by the algorithm) within a series of recorded images. In other words, unfocused or overlapped bubbles in neglected image can yield discontinuous measured time series. Therefore, it is proper to use edge eroded image but, there could be errors caused by coalesced bubbles. As shown in Figure 5, couple of points are located in the image at 375 mm above the bottom of the tank. The representative bubble velocity is determined by cross-correlation between two binary signals extracted from the two points. Figure 6 shows two different time series signals extracted from the top ($U$) and bottom ($B$) sides of the line. Pairs of bubble signals have local characteristic time lags relative to each other (i.e., $\tau_1$, $\tau_2$, $\tau_3$, …, $\tau_M$), but we select a representative time lag by calculating the cross-correlation coefficient between a pair of signals as follows:

$$R_{xy}(\tau) = \frac{1}{N}\int_{-\infty}^{\infty} U(t)B(t-\tau)\ dt \qquad (6)$$

The following is for a discrete time series:

$$R_{xy}(mT) = \frac{1}{N}\sum_{n=0}^{N-1} U(nT)\ B(nT - mT) \qquad (7)$$

where $N$ is the total number of frames, $nT$ corresponds to a specific time $t$, and $mT$ is the time lag ($\tau$). When the maximum $R_{xy}$ occurs, the time lag is called the representative time lag ($\tau_{max}$). To obtain velocity profiles over the horizontal locations, couples of extraction points are placed in each pixel. The representative bubble velocity at each horizontal pixel is determined as follows:

$$u_{b,j} = \frac{y}{\tau_{max,j},j} \qquad (8)$$

where $u_{b,j}$ is representative bubble velocity at $j$-th pixel, $y$ is vertical gap between two points, and $\tau_{max,j}$ is representative time lag at $j$-th pixel. The vertical gap between two points ($y$) is specified carefully due to following reasons: (1) small bubble cannot detected by coupled two points with large gap because of its lateral motions (2) not enough gap results in too low resolution of velocity profiles due to frame rates are fixed as 1000 fps. The value of y is given as 60 ~ 90 pixels considering the bubble velocity in each case. After obtaining velocity profiles, erroneous velocities with infinite values occurred between 10 and 40 of the extraction points (out of 600 to 800 points within validated range) due to division by zero by zero or near-zero values of $\tau_{max,j}$. This gives an estimated 6.7% maximum uncertainty in the velocity profile. After removing erroneous velocity data, velocity profiles with of the various conditions are composed of velocities with magnitudes of 0.3 ~ 0.9 m/s of bubble velocity.

The region of the image where a few small bubbles pass can cause erroneous velocity values due to the discordance of the two signals. In other words, the lateral motion of tiny bubbles cannot be detected by two detection points. Hence, the valid range should be trimmed to exclude erroneous region using the estimation of the void fraction ($\alpha$). $\alpha$ is determined by the summation of signals at each extraction point and equals to cross-correlation coefficient with representative time lag at each extraction point. The valid range is defined based on the cumulative distribution function of $\boldsymbol{\alpha}$:

$$\boldsymbol{\beta}_{valid,\mathrm{j}} = \begin{cases} \mathbf{0} & \boldsymbol{\alpha}_{\mathrm{j}} \in \mathrm{CDF}(\boldsymbol{\alpha}_{\mathrm{j}}) < \mathbf{0.1} \\ \mathbf{1} & \boldsymbol{\alpha}_{\mathrm{j}} \in \mathbf{0.1} \leq \mathrm{CDF}(\boldsymbol{\alpha}_{\mathrm{j}}) \leq \mathbf{0.9} \\ \mathbf{0} & \boldsymbol{\alpha}_{\mathrm{j}} \in \mathrm{CDF}(\boldsymbol{\alpha}_{\mathrm{j}}) > \mathbf{0.9} \end{cases} \tag{9}$$

$$\boldsymbol{where},\ \boldsymbol{\alpha}_{j} = \frac{\mathbf{1}}{\boldsymbol{N}} \sum_{\mathrm{n}=0}^{\boldsymbol{N}-1} \mathrm{U(nT)\ B(nT} - \boldsymbol{\tau}_{\boldsymbol{M}})$$

$\mathrm{CDF}(\alpha)$ means cumulative distribution function of $\alpha$ along horizontal pixels. The binary column vector $\beta_{valid,\mathrm{j}}$ specifies the spatially valid range of the velocity profile. Figure 7 shows the velocity profiles from the presented valid range. For the high-flowrate cases with water injection (10 L/min and 15 L/min), the velocity profile extraction cannot be achieved because the void fractions are too high.

## 4. Results and discussion

### 4.1. Bubble size distribution

Figure 8 shows the probability density function (PDF) of the bubble size in the range of 0 - 20 mm as a line graph. All cases show poly-dispersed distribution of bubble equivalent size, but there were distinct differences of bubble characteristics generated from each case. The bubble size distribution of cases with the air-driven ejector and plain nozzle show more skewed distributions toward the left, and the most dominant probability of bubble size is around 1.5 mm. As the air flowrate increases, more conspicuous peak value is observed. The dominant probability in the case with water injection is slightly larger (2 mm). However, there was a significant difference between the former cases and the water injection case in terms of bubble generating mechanism resulting in different size of bubbles and different number of bubbles.

The bar graph in Figure 8 shows the number of bubbles generated in each case. When the air flowrate is 2 L/min, nearly 8 times more bubbles are generated in the water injection case. The other cases cannot sufficiently break up the bubbles, and large bubbles are formed. As the flowrate increases, the number of bubbles with water injection becomes smaller. This results from massive overlaps that occur at the graphical plane. These overlapped bubbles are discarded by image processing criteria as expressed in equation 5. Except for neglected bubbles, bubble size distributions are remained. This implies that the essentials of bubble generation mechanism in each case are not significantly changed.

To support this interpretation, the bubble size histogram is used to calculate the Sauter mean diameter, which can characterize the efficiency of a mixing process as a ratio of the volumetric to the superficial geometry as follows:

$$d_{32} = \frac{\sum_{i=1}^{N} n_i d_{b,eq,i}^{3}}{\sum_{i=1}^{N} n_i d_{b,eq,i}^{2}} \qquad (10)$$

The Sauter mean diameters of each case are shown in Figure 9 (a). The Sauter mean diameter of the plain nozzle case and air-driven ejector case gradually increased as the air flow rate increased. However, in the case with water injection, the Sauter mean diameter does not vary significantly. These tendencies are caused by the different bubble generating mechanisms in each case.

In the plain nozzle and the air-driven ejector cases with moderate air flowrate, large bubbles are ergodically detached from the nozzle and oscillate along the streamwise direction. Also, small bubbles can be detached from the nozzle but, surface instabilities on the large bubble can break up the bubble itself and generate variety size of bubbles. Furthermore, entrainment and wake induced by leading large bubble cause break up of following large bubble. To support our report on bubble characteristics, graphically depicted motions of large bubble in the case of plain nozzle is shown in Figure 10 and Figure 11. Figure 10 shows that leading large bubble are rising with lateral motion around centerline and many small bubbles are breaking off the large bubble. Meanwhile, following bubble's lateral motion is driven by leading bubble and causes bubble break-up, consequently [23, 36]. Figure 11 shows the snapshots of the case with plain nozzle with different air flowrate. In the highest flowrate case, lots of discharging air results in coalesced irregular swarm of bubbles as shown in bottom side of Figure 11 (d). From these irregular bubbles, bubble break up phenomena occur simultaneously around the flow field. Thus, small bubbles can be uniformly distributed. This also can be proved by the Probability Density Functions obtained from separated radial and axial sections as shown in Figure 12. Radial and axial BSD (bubble size distribution) is collected from three sections which have same width and height respectively. In the case of plain nozzle and air-driven ejector cases, BSD for radial sections at the low air flowrate case (Figure 13 (a), (b)) show small bubbles are concentrated on outer section. In the high air flowrate condition (Figure 13 (d), (e)), BSD for axial sections are almost identical with each other. It is influence of mixing characteristics caused by intense large bubbles' lateral motions at high air flowrate condition. Furthermore, BSD for axial sections (Figure 14 (a), (b), (d), (e)) show that relatively small bubbles are concentrated on top section, but large bubbles are concentrated on bottom section. This fact projects that coalescence of bubble at the lower section of flow field and small bubbles break apart from the large, coalesced bubble at the higher section of flow field. As a result, the Sauter mean diameter of the case with the plain nozzle and the air-driven ejector gradually increased under the influence of increasing number of large bubbles as the flowrate increases.

In the ejector with water injection case, small bubbles are formed through the suction and mixing chamber. This mechanism makes different tendency of bubble distribution with former cases. As shown in BSD for radial and axial sections with water injection, (Figure 13 (c), (f)) outer section contains most of small bubbles and this characteristic is still remained even in high air flowrate condition. From the BSD for axial sections (Figure 14 (c), (f)), we can expect that coalesced bubbles in high air flowrate condition are going to be dispersed toward horizontally as the flow goes up. In other words, bubble swarm generated from the ejector with water injection shows self-similarity based on uniformly sized bubbles. This is in accordance with previous researches. Fujiwara et al. and Zheng et al. [12, 14] reported, because relationship between the amount of gas flowrate and bubble size distribution is very small, uniformly sized bubbles can come out of the ejector with water injection. Literature and the result from this study show that the mechanism generating bubbles in the case with water injection has robustness with the amount of supplied air. Regarding bubble size distribution, there are always center peaked distribution with all of air flowrate cases because uniformly sized bubbles are discharged from ejector, undergo swirl effect and turbulent dispersion to push agglomerated bubbles toward spanwise direction, and finally form a plume like bubble swarm. As a result, the case with water injection eventually produces bubble swarm with smaller bubbles and wider dispersion angle than former cases and results in similar values of Sauter mean diameter with different air flowrate cases.

### 4.2. Bubble rise velocity

Figure 15 shows the moving average bubble rise velocity profiles calculated with 63 adjacent points around each pixel point. Figure 15 (a) compares bubble representative velocity profiles extracted from the center of FOV as described in Section 3.2. In Figure 15 (b) ~ (d), two additional velocity profiles are extracted from the each top and bottom side of FOV. The case with water injection shows low velocity profiles at bottom side of FOV because the swirl effect of the ejector results in energy losses. Due to the fact that water injection is achieved with inserted 8 mm nozzle in Figure 1 (b), bubbles generated from the water injection case show revolving motions around centerline at the bottom of FOV and this swirl effect is gradually dissipated as shown in Figure 16. In present study, we designed the ejector to compare each case. However, the design of ejector should be enhanced toward removing the swirl effect to enhance bubble characteristics (e.g. water injection from the bottom of the ejector). As reported by Zheng et al. [14], their swirl body inside ejector caused more energy consumption, larger bubble size, smaller interfacial area, and lower gas hold-up.

Generally, the case with water injection shows wider and lower velocity profiles than the other cases. The bubbles in the plain nozzle and air-driven ejector case are larger, but the velocity profiles have higher values than in the water injection case. This occurs because large bubbles are detached from each bubble-generating system, and accompany entrainment, causing the acceleration of the surrounding and following smaller bubbles. This phenomenon causes the observed increase in the bubble rise velocity profiles.

From the validated velocity profiles obtained from equation 8, the mean velocity is calculated as follows:

$$u_b = \frac{\sum_{i=1}^{N} u_{b,j}\alpha_j}{\sum_{i=1}^{N} \alpha_j} \quad (11)$$

where $u_{b,j}$ and $\alpha_j$ are the bubble rise velocity and void fraction at the $j$-th pixel, respectively. The mean velocity is calculated from the velocity profiles with the void fraction of each extraction point as weighting factors. Figure 9 (b) shows the mean bubble rise velocity of each case. All cases show an increase of bubble velocity as the air flowrate increases. The increase of rise velocity can be interpreted with the different points of view already discussed in section 4.1 for each case: (1) for plain nozzle and air-driven ejector case, it is induced by large bubbles motion and local entrainment (2) for the ejector with water injection case, it is caused by enhanced turbulent around the overall flow field. As a result, the bubble rise velocity in the case with water injection is lower than in other cases, but the difference between the cases does not exceed 10%.

### 4.3. Demonstration with a spherical model

It is expected that the case with water injection will show better momentum transfer performance because there is no significant difference in the bubble rise velocity between each case, but uniform bubble size distribution and large dispersion angle are achieved in the case with water injection. To verify the difference in performance between each case, a buoyancy experiment with a spherical model was conducted.

Figure 17 (a) shows a diagram of the experiment, and Figure 17 (b) shows the spherical model in the bubble swarm generated in the cases with the ejector. The experiment was conducted with a 50-mm acrylic sphere filled with adhesive. The density of the spherical model was adjusted to a specific gravity (SG) of 1.15. The motion of the model was captured by a high-speed camera at 60 fps and a duration of more than 150 s. The position of the model was calculated using the cross-correlated binary signal between each image, which was stored in the memory. The model trajectories are shown in Figure 18.

Figure 19 shows the PDF of the position obtained at air flow rates of 10 L/min and 15 L/min. When the air flowrate is 10 L/min, only the case with water injection can lift the model. Even when the air flowrate increased to 15

L/min, the PDF of the plain nozzle and air-driven ejector cases still remained skewed toward the left. However, the buoyant performance of the case with water injection was good at both 10 L/min and 15 L/min. The experiment revealed two mechanisms influencing the motion of the spherical model: (1) instantaneous motion of spherical model caused by large bubbles in plain nozzle and air-driven ejector cases, and (2) steady motion of spherical model caused by evenly distributed bubbly flow in ejector with water injection case. In former cases, large bubble contributes to lift the spherical model by inducing the entrainment of surrounding liquid upwards and inducing virtual mass forces top side of the model. Nevertheless, if the bubble has contact with the bottom side of the model, sudden sinking will result due to lower air density when compared to water. Consequently, those instantaneous forces cannot sustain the lift on the model against gravitational forces. Meanwhile, there are not only vertical forces, but also lateral forces caused by large bubbles. Hence, effect of virtual mass forces and history forces is realized as a series of instantaneous lateral motions of spherical model as shown in Figure 18 (a) and (b). In the latter case, however, there is drag force exerted on the model by developed turbulent bubbly flow toward up. Drag force is induced by evenly distributed bubbles and gradually decreases as the flow goes to downstream or in the spanwise direction. In Figure 18 (c) the spherical model is steadily lifted by the flow until it deviates from the main stream of flow.

### 4.4. Bubble swarm characteristics and comparison with literature

As gas flowrate increases, bubbles generally changed from elliptical to spherical shapes. Second-order moments were calculated and used to determine bubble aspect ratio [23]. Figure 20 shows the probability density function of aspect ratio of (a) smaller and (b) larger bubbles in each case. For small bubbles, especially in the case with water injection, remarkable change of aspect ratio occurs as the air flowrate increases. But for large bubbles, there are no significant changes in the aspect ratio. This is consistent with observations by Besagni and Inzoli [28], and Ziegenhein and Lucas [28, 37]. Besagni and Inzoli [28] report that increase in gas superficial velocity caused significant changes in aspect ratio distribution. In the highest superficial velocity of gas case, transition of flow regime from homogeneous bubbly flow induced more distorted and spherical shape of bubbles. Ziegenhein and Lucas [37] showed that the ‘Airlift’ case in their study, where the highest turbulence was observed, produced higher aspect ratios. But all cases produced distributions that similarly peaked at an aspect ratio range of 0.5–0.6.

In the case of water injection in the present study, in low air flowrate conditions, there was not sufficient turbulence to substantially deform bubbles. However, as the air flowrate increases, turbulence is enhanced, and distorted spherical bubbles are produced. In the plain nozzle and air-driven ejector cases, however, small trailing bubbles are more spherical than ellipsoidal especially in the immediate wake of the large bubbles detached from the nozzle. We observe that the wake of each large bubble is more turbulent than in front of it, but turbulence is perhaps more evenly distributed in the case where bubbles are more finely distributed such as with the water-injected ejector. Therefore, the latter case is more a desirable method of generating bubble swarms for enhancing uniform momentum transport performance.

In previous literatures, there were many attempts to predict the aspect ratio of bubbles in the columns [22, 28, 37, 38]. They preference is to compare relationships between Eo, We, Re and aspect ratio using correlations. These dated back to the studies of Moore [39], Taylor and Acrivos [40], and Wellek et al. [41]. Eötvös number correlations were used to compare the aspect ratio of the present study and literatures. Calculated aspect ratios for each condition were averaged for comparison. Comparison was done with the correlation of Wellek et al. [41] which was obtained from single bubbles in contaminated water; the correlation of Okawa et al [30] which was obtained by modifying the correlation of Wellek et al. [41] using the lower boundary of their data; and the correlation of Besagni and Inzoli [28] which was obtained by modifying previous correlations for their bubble data from bubble column. Figure 21 shows the comparison of these correlations with the current data of aspect ratios at experimental gas flowrates 2 and 15 L/min. The correlations of Wellek et al. [41] and Okawa et al. [42] showed overestimated and underestimated aspect ratio, respectively. Although overall underestimated prediction was observed from the correlation of Okawa et al. [42], it fitted experimental results with very low Eo values. For the correlation of Besagni and Inzoli, it better fitted result with the case of plain nozzle and the case of air-driven ejector at low air flowrate conditions. At the high air flowrate conditions, experimental data showed flatter tendency in high Eo region. So, we revised the correlation considering the amount of air ejected from the nozzle as follows:

$$\mathbf{E} = \frac{\mathbf{1}}{(\mathbf{1} + \mathbf{1.014} \times \boldsymbol{Eo}^{\mathbf{0.11}} \times \boldsymbol{Re}^{-\mathbf{0.06}})} \qquad \mathbf{(12)}$$

where E is the aspect ratio, Eo is the bubbles' Eötvös number, and Re is Reynolds number at the exit of the nozzle. However, the result of the case with water injection showed quite different tendency with other cases and it cannot be defined with conventional correlations. We note the similarity of Equation 12 with that reported by Zigenhein and Lucas [37]; they used bubble terminal velocity obtained from single bubbles in their experiments and dealt with small and large bubbles separately as was also done in the current investigation. However, characterizing bubble swarms generated from the ejector with water injection is an important subject to resolve in the future studies.

## 5. Conclusion

An ejector with water injection was presented in this study to generate the bubble swarm with evenly sized bubbles, and wider dispersion angle. Also, presented method performs enhanced momentum transfer characteristics. In this study, bubble swarms were generated with three different cases: (1) a plain nozzle, (2) and air-driven ejector, and (3) an ejector with water injection. Bubble visualization was achieved with high-speed photography and a series of digital image processes to distinguish individual bubbles on the focal plane. There was a decrease in the number of bubbles detected due to the massive bubble overlap in the water injection case as air flowrate increases. Therefore, for comparison between each case quantitatively and qualitatively, the bubble size distribution, bubble aspect ratio, Sauter mean diameter, representative bubble velocity, and buoyancy performance were examined to compare the characteristics of bubble swarms generated in each case.

The generated number of bubbles in the water injection case was remarkable, as seen in the bubble swarm snapshots. When the air flowrate is 2 L/min, the case with water injection produces finely-sized bubbles nearly 8 times more than other cases. It showed visually similar performance to that produced by bubble generators such as the sparger used by Besagni and Inzoli. However, the ejector with water injection showed consistencies on bubble size PDF as the air flowrate increases. But the increase of air flowrate induced high turbulence in the flow field and caused more spherical bubble shape and increase of rise velocity of bubbles. From the result, the ejector can be better way to generate bubble swarms because there is huge pressure drop across the sparger's holes, however this the ejector can result in lesser energy costs and evenly sized bubble distribution with wider dispersion angle.

In terms of the bubble generating mechanism, the plain nozzle and air-driven ejector cases make ergodically large bubbles, and many small bubbles break apart from the large bubbles. This caused small separated bubbles, but large bubbles still remained and contributed to the large value of the Sauter mean diameter and higher values of the velocity profiles. However, in the case with water injection, small bubbles were generated through the suction and mixing chamber inside the ejector, and evenly distributed broken-up bubbles came out. Even though the most dominant size of the bubble is larger than in the other cases, the uniformly sized bubbles resulted in a small Sauter mean velocity and moderate rise velocity. We also measured bubble rise velocity near the ejector as well as at further locations. In the case of water injection, there was a swirl effect near the ejector which can result in more energy consumption, larger bubbles and lower bubble velocities. But the swirl effect diminishes as bubbles rise and become more evenly distributed. To enhance bubble characteristics, swirl effect should be decreased, and it may be achieved by reviewing the methodology for injecting water inside the ejector. Finally, the case with water injection shows better buoyancy performance than the other cases. This results from the uniformly-sized bubbles, which lead to higher momentum exchange between the bubbles and the surrounding water.

**Acknowledgement**

This work was also supported by the National Research Foundation of Korea (NRF) grant funded by the Korean government (MSIT) (No. 2011-0030013, No. 2018R1A2B2007117).

**Nomenclature**

***Symbols***

| | |
|---|---|
| $A_{b,I}$ | Area of the *i*-th bubble in binary image |
| $B_j$ | Binary signal extracted from bottom side of j-th extraction pair. |
| $b_i$ | Position of pixels consisting of *i*-th bubble in binary image |
| $d_{b,eq,i}$ | Equivalent diameter of i-th bubble in binary image |
| $d_{32}$ | Sauter mean diameter |
| E | Aspect ratio of bubble |

| | |
|---|---|
| I | Grayscale image of bubbles |
| J | Maximum horizontal pixel number |
| K | Number of bubbles passing specific pair of extraction points |
| m | Integer number within $0 \sim \mathrm{N} - 1$ |
| N | Total number of frames |
| n | Frame number |
| P | Prewitt method mask |
| $p_i$ | Perimeter of i-th bubble in binary image |
| $p_{i,sphere}$ | Equivalent perimeter of i-th bubble in binary image |
| $R_{xy}$ | Cross-correlation coefficient |
| $s_1$ | The first shape factor |
| $s_2$ | The second shape factor |
| $t$ | Specified time |
| $T$ | Temporal resolution according to 1/fps. |
| $U_j$ | Binary signal extracted from top side of j-th extraction pair |
| $u_b$ | Mean bubble velocity |
| $u_{b,j}$ | Representative bubble velocity at j-th pixel |
| $u_g$ | Velocity of air at the nozzle |
| $y$ | Vertical gap between pair of extraction points |
| $\alpha_j$ | Estimation of void fraction at j-th pixel |
| $\beta_{valid,j}$ | Validity of representative velocity extracted by extraction points at j-th pixel (1, 0) |
| $\tau_{max,j}$ | Representative time lag at j-th pixel |

***Non-dimensional numbers***

| | |
|---|---|
| Eo | Bubble Eötvös number |

| | |
|---|---|
| Re | Reynolds number at the exit of nozzle |

***Abbreviation***

| | |
|---|---|
| BSD | Bubble size distribution |
| CDF | Cumulative distribution function |
| FOV | Field of view |
| fps | Frame per second |
| PDF | Probability density function |

***Subscripts***

| | |
|---|---|
| *b* | Bubble |
| *eq* | equivalent value for the bubble as spherical shape |
| *h* | horizontal |
| *i* | Assigned number for labelled bubble |
| *j* | Horizontal position of pair of extraction points (pixel) |
| *k* | Order of bubbles passing specific extraction points |
| *o* | original |
| *v* | vertical |
| *max* | Maximum |
| *sphere* | Assumption that the bubble is spherical shape |

## References


[1] Temesgen T, Bui TT, Han M, il Kim T, Park H. Micro and nanobubble technologies as a new horizon for water-treatment techniques: A review. Advances in Colloid and Interface Science. 2017;246(June):40--51.

[2] Hanselmann W, Windhab E. Flow characteristics and modelling of foam generation in a continuous rotor/stator mixer. Journal of Food Engineering. 1998;38(4):393--405.

[3] West A, Brooks NH, Imboden DM. Bubble plume modeling for lake restoration. Water Resources Research. 1992;28(12):3235--50.

[4] Hamed M. Hydrodynamics, Mixing, and Mass Transfer in Bubble Columns with Internals. 2012:145.

[5] Patankar SV, Spalding DB. Momentum Transfer in Three-Dimensional: Pergamon Press Ltd, 1972.


ACCEPTED MANUSCRIPT

[6] Kulkarni AA, Joshi JB. Bubble formation and bubble rise velocity in gas-liquid systems: A review. Industrial and Engineering Chemistry Research. 2005;44(16):5873--931.
[7] Kulkarni AV, Joshi JB. Design and selection of sparger for bubble column reactor. Part I: Performance of different spargers. Chemical Engineering Research and Design. 2011;89(10):1972--85.
[8] Thorat BN, Shevade AV, Bhilegaonkar KN, Aglawe RHa. Effect of Sparger Design and Height to Diameter Ratio on Fractional Gas Hold-up in Bubble Columns. Chemical Engineering Research and Design. 1998;76(7):823--34.
[9] Chen J, Jarall S, Havtun H, Palm B. A review on versatile ejector applications in refrigeration systems. Renewable and Sustainable Energy Reviews. 2015;49:67--90.
[10] Cramers PHMR, Beenackers AACM, van Dierendonck LL. Hydrodynamics and mass transfer characteristics of a loop-venturi reactor with a downflow liquid jet ejector. Chemical Engineering Science. 1992;47(13-14):3557--64.
[11] Dutta NN, Raghavan KV. Mass transfer and hydrodynamic characteristics of loop reactors with downflow liquid jet ejector. The Chemical Engineering Journal. 1987;36(2):111--21.
[12] Fujiwara A, Takagi S, Watanabe K, Matsumoto Y. Experimental study on the new micro-bubble generator and its application to water purification system. SME/JSME 2003 4th Joint Fluids Summer Engineering Conference. 2003:469--73.
[13] Yin J, Li J, Li H, Liu W, Wang D. Experimental study on the bubble generation characteristics for an venturi type bubble generator. International Journal of Heat and Mass Transfer. 2015;91:218--24.
[14] Zheng SQ, Yao Y, Guo FF, Bi RS, Li JY. Local bubble size distribution, gas-liquid interfacial areas and gas holdups in an up-flow ejector. Chemical Engineering Science. 2010;65(18):5264--71.
[15] Doherty JA, Verma RS, Shrivastava S, Saxena SC. Heat transfer from immersed horizontal tubes of different diameter in a gas-fluidized bed. Energy. 1986;11(8):773--83.
[16] Saxena SC, Vadivel R. Heat transfer and hydrodynamic studies in gas-fluidized beds. Energy. 1989;14(6):353--62.
[17] Azimi SS, Kalbasi M. Three-phase modeling of dehydrogenation of isobutane to isobutene in a fluidized bed reactor: Effect of operating conditions on the energy consumption. Energy. 2018;149:250--61.
[18] Shuping Z, Yulong W, Mingde Y, Kaleem I, Chun L, Tong J. Production and characterization of bio-oil from hydrothermal liquefaction of microalgae Dunaliella tertiolecta cake. Energy. 2010;35(12):5406--11.
[19] Chen Q, Ja MK, Li Y, Chua KJ. Energy, economic and environmental (3E) analysis and multi-objective optimization of a spray-assisted low-temperature desalination system. Energy. 2018;151:387--401.
[20] Rajaseenivasan T, Shanmugam RK, Hareesh VM, Srithar K. Combined probation of bubble column humidification dehumidification desalination system using solar collectors. Energy. 2016;116:459--69.
[21] Kim YK, Lee DY, Kim HD, Ahn JH, Kim KC. An experimental and numerical study on hydrodynamic characteristics of horizontal annular type water-air ejector. Journal of Mechanical Science and Technology. 2012;26(9):2773--81.
[22] Liu L, Yan H, Zhao G. Experimental studies on the shape and motion of air bubbles in viscous liquids. Experimental Thermal and Fluid Science. 2015;62:109--21.
[23] Ravelet F, Colin C, Risso F. On the dynamics and breakup of a bubble rising in a turbulent flow. Physics of Fluids. 2011;23(10).
[24] Busciglio A, Vella G, Micale G, Rizzuti L. Analysis of the bubbling behaviour of 2D gas solid fluidized beds. Part I. Digital image analysis technique. Chemical Engineering Journal. 2008;140(1-3):398--413.
[25] Shen L, Johnsson F, Leckner B. Digital image analysis of hydrodynamics two-dimensional bubbling fluidized beds. Chemical Engineering Science. 2004;59(13):2607--17.
[26] Sadr-Kazemi N, Cilliers JJ. An image processing algorithm for measurement of flotation froth bubble size and shape distributions. Minerals Engineering. 1997;10(10):1075--83.
[27] Lau YM, Deen NG, Kuipers JAM. Development of an image measurement technique for size distribution in dense bubbly flows. Chemical Engineering Science. 2013;94:20--9.
[28] Besagni G, Inzoli F. Bubble size distributions and shapes in annular gap bubble column. Experimental Thermal and Fluid Science. 2016;74:27--48.
[29] Ziegenhein T, Zalucky J, Rzehak R, Lucas D. On the hydrodynamics of airlift reactors, Part I: Experiments. Chemical Engineering Science. 2016;150:54--65.
[30] Xu Y, Aliyu AM, Seo H, Wang JJ, Kim KC. Effect of crossflow velocity on underwater bubble swarms. International Journal of Multiphase Flow. 2018;0:1--14.
[31] Aliyu AM, Seo H, Kim M, Kim KC. An experimental study on the characteristics of ejector-generated bubble swarms. Journal of Visualization. 2018:1--18.

[32] Aliyu AM, Seo H, Kim H, Kim KC. Characteristics of bubble-induced liquid flows in a rectangular tank. Experimental Thermal and Fluid Science. 2018;97(November 2017):21--35.
[33] Aliyu AM, Seo H, Xu Y, Wang J-J, Kim KC. A model for rising bubbles interacting with crossflowing liquid. International Journal of Multiphase Flow. 2018.
[34] Prewitt JM. Object enhancement and extraction. Picture processing and Psychopictorics. 1970;10(1):15-9.
[35] Ishii M, Kim S, Uhle J. Interfacial area transport equation: Model development and benchmark experiments. International Journal of Heat and Mass Transfer. 2002;45(15):3111--23.
[36] Ellingsen K, Risso F. On the rise of an ellipsoidal bubble in water: oscillatory paths and liquid-induced velocity. J Fluid Mech. 2001;440:235--68.
[37] Ziegenhein T, Lucas D. Observations on bubble shapes in bubble columns under different flow conditions. Experimental Thermal and Fluid Science. 2017;85:248--56.
[38] Celata GP, Cumo M, D'Annibale F, Tomiyama A. The wake effect on bubble rising velocity in one-component systems. International Journal of Multiphase Flow. 2004;30(7-8 SPEC. ISS.):939--61.
[39] Moore DW. The velocity of rise of distorted gas bubbles in a liquid of small viscosity. Journal of Fluid Mechanics. 1965;23(4):749--66.
[40] Taylor TD, Acrivos A. On the deformation and drag of a type-A multiple drop at low Reynolds number. Journal of Fluid Mechanics. 1963;1964(18):466.
[41] Wellek RM, Agrawal AK, Skelland AHP. Liquid Media. 1966;245(10):237--45.
[42] Okawa T, Tanaka T, Kataoka I, Mori M. Temperature effect on single bubble rise characteristics in stagnant distilled water. International Journal of Heat and Mass Transfer. 2003;46(5):903--13.

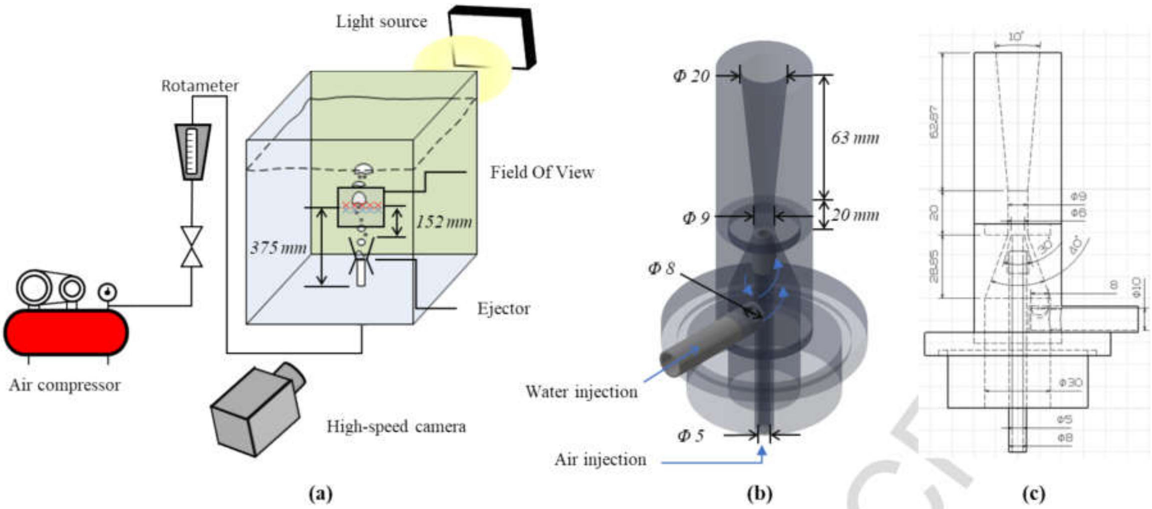


595

596 **Figure 1. Overall experimental setup: (a) Configuration of equipment, (b) Ejector geometry, (c) Draft for**
597 **fabrication of the ejector**

598

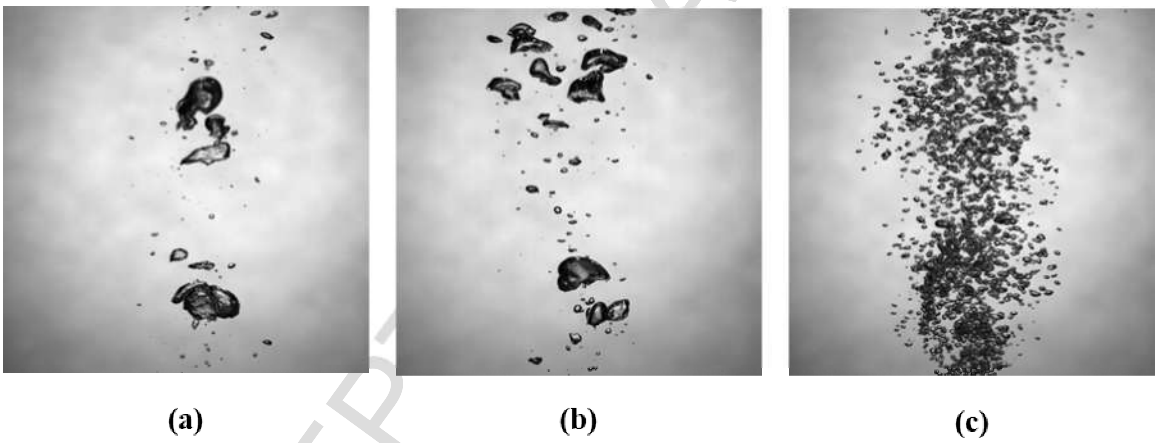


599

600 **Figure 2. Snapshot of bubble swarms in each case: (a) Plain nozzle, (b) Air-driven ejector, (c) With water**
601 **injection at the air flowrate with 3 L/min**

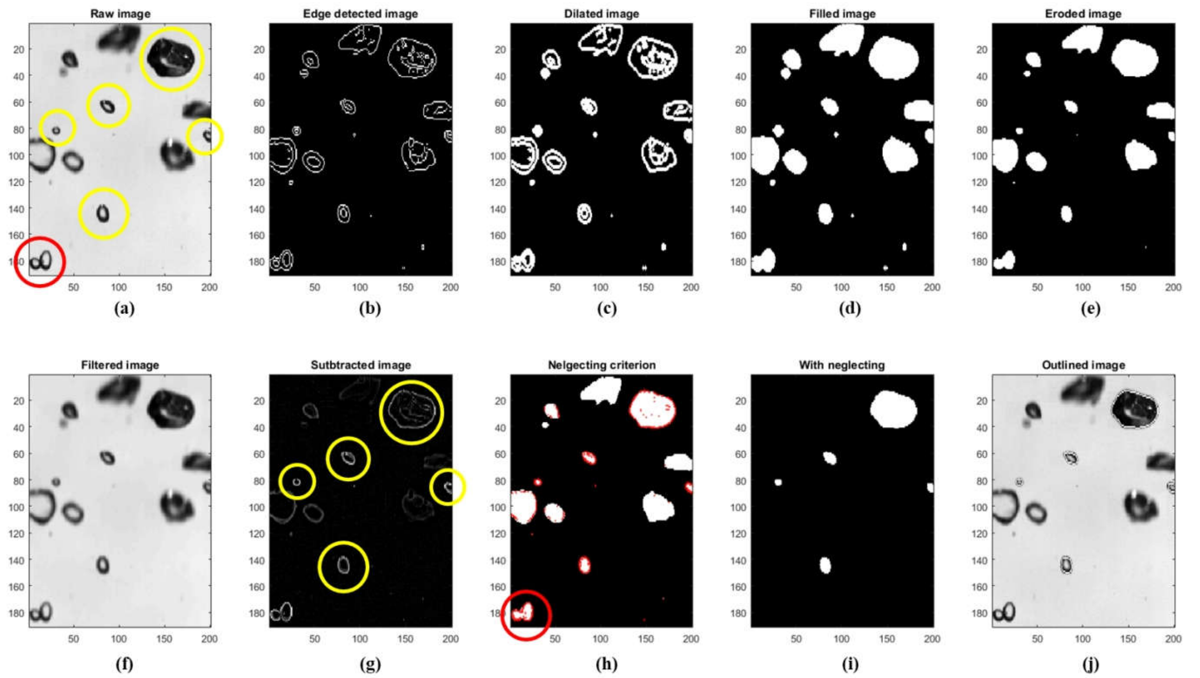


**Figure 3. Image processing procedure with filtering out bubbles: (a) Raw bubble image, (b) Lined bubble image with Prewitt method, (c) Edge dilated image, (d) Hole filled image, (e) Edge eroded, (f) Gaussian filtered image, (g) raw image subtracted by gaussian filtered image (expressed with normalized intensity), (h) Bubble edges shared between e and g, (i) bubble image after discarding bubbles, (j) Outlined raw image**

**Figure 4. Example of labelled image of bubbles (original image is shown in Figure 3 (a))**

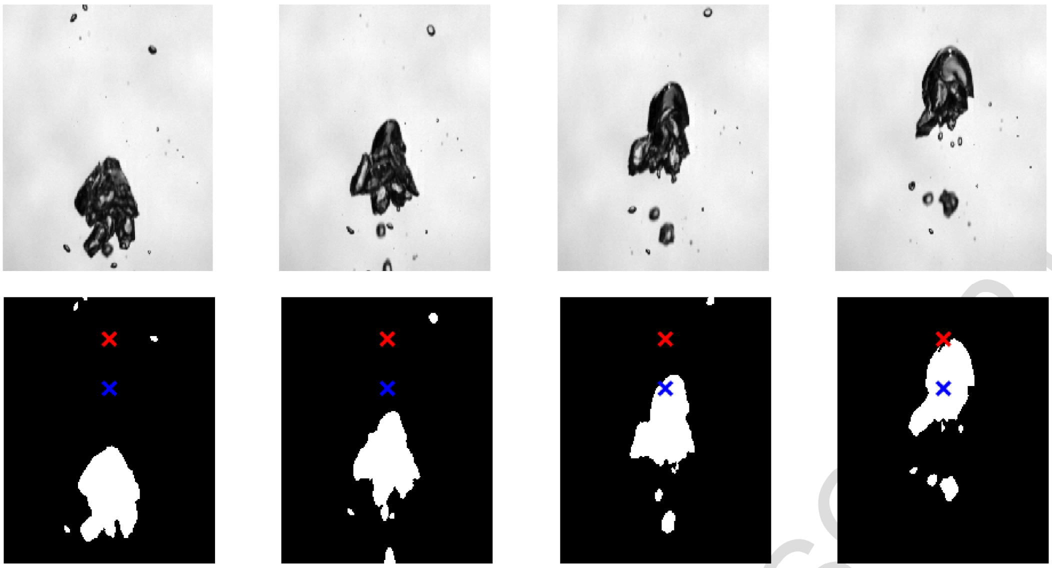

**Figure 5. Binary signal extraction from two points (up: raw images, down: binarized images from edge eroding process, time interval with 30/2000 s)**

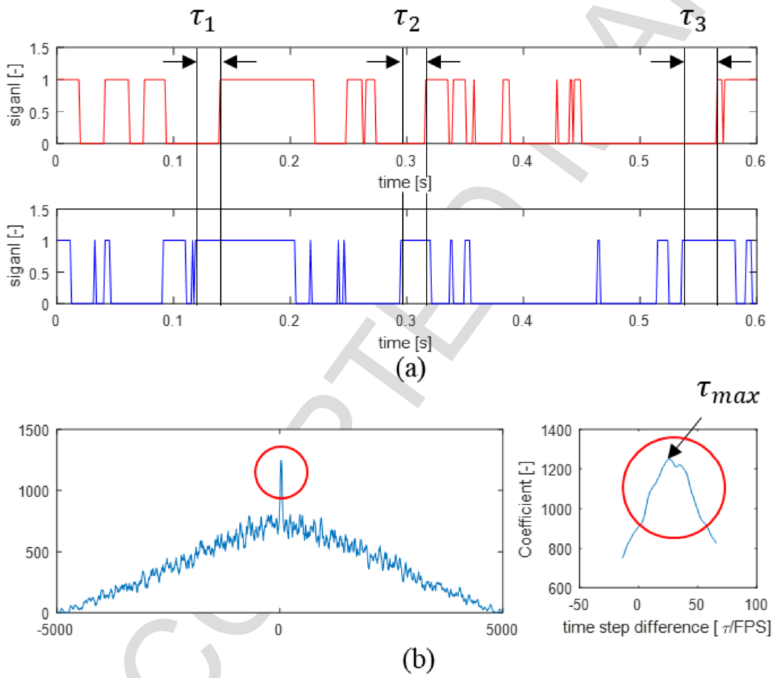


**Figure 6. Velocity determination by cross-correlated coefficient: (a) Two binary signal from two extraction points, (b) Cross-correlation coefficient of two signals**

616 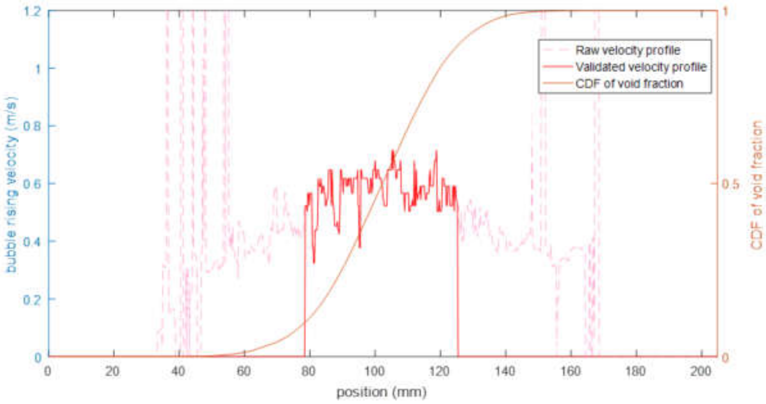


617 **Figure 7. Validation of representative bubble velocity profile**

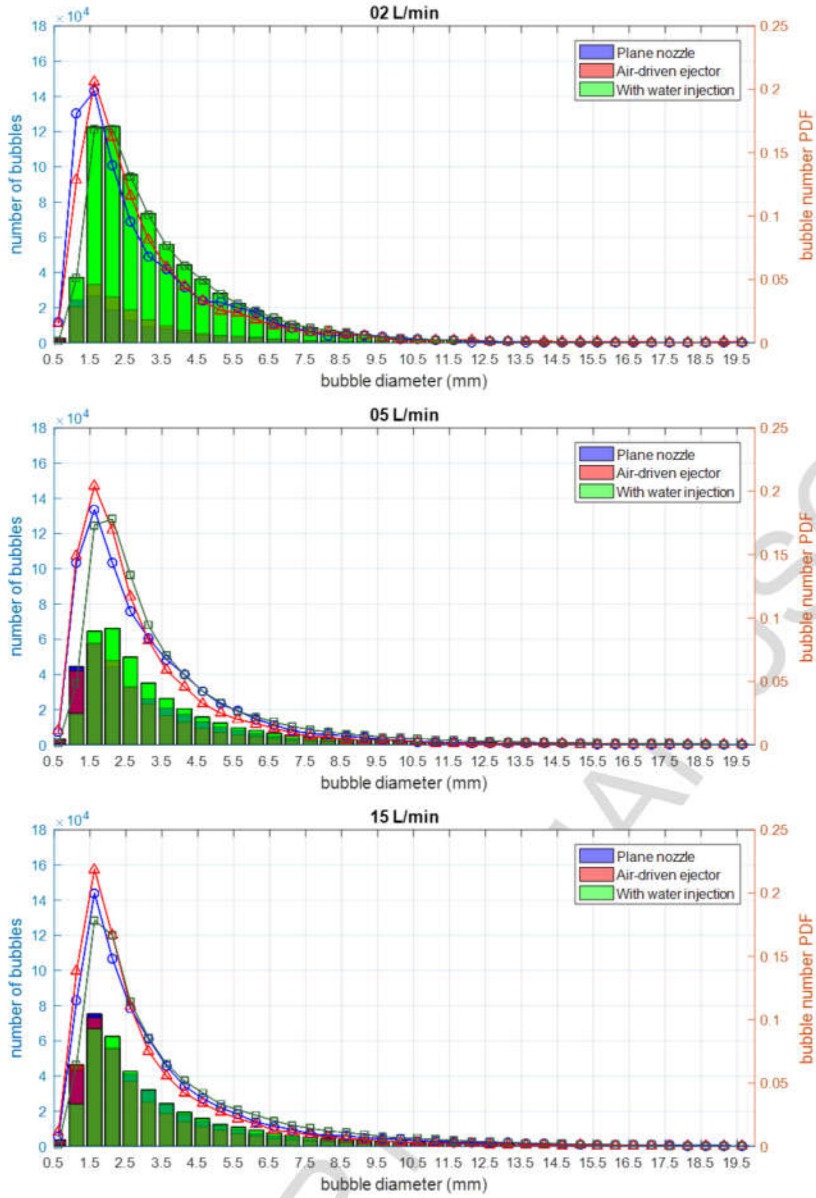


**Figure 8. Number of bubbles (bar) and probability density function (line) in each case**

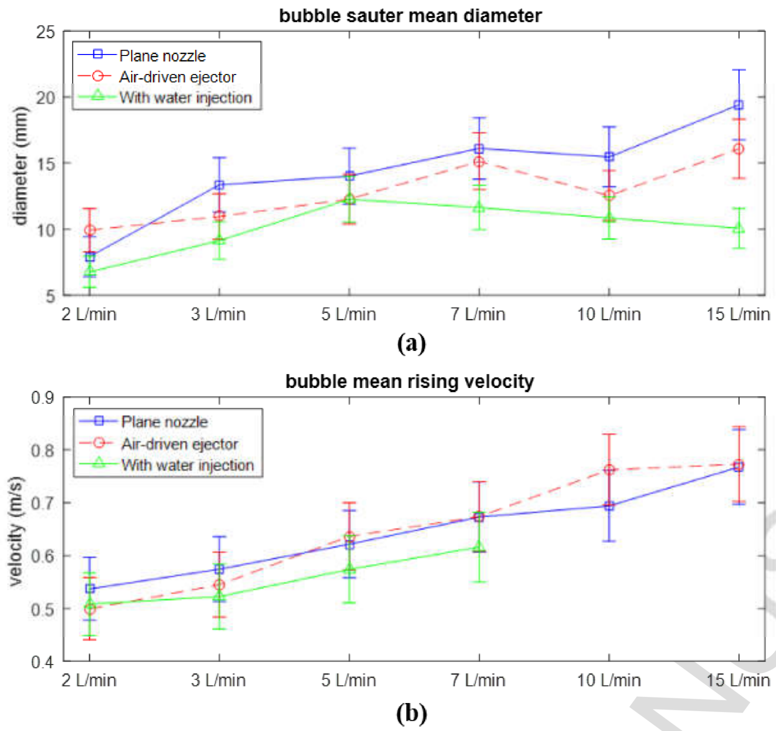


**Figure 9. Variation of: (a) Sauter mean diameter and (b) Equivalent bubble rising velocity in each case**

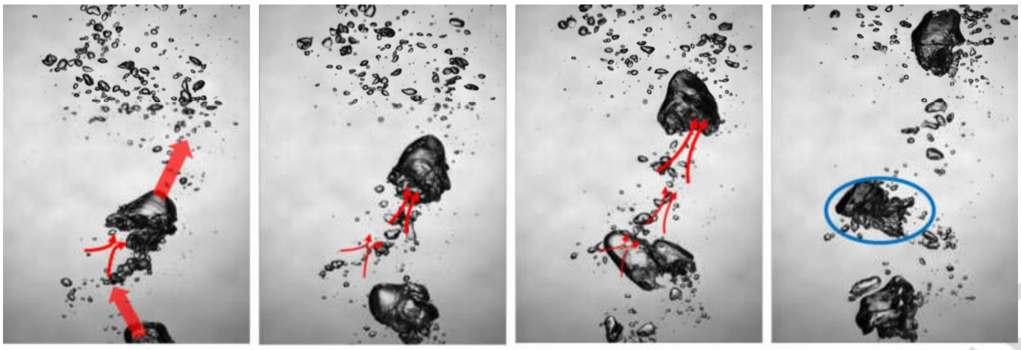

(a) (b) (c) (d)

**Figure 10. Bubble break-up and lateral motions in the case of plain nozzle for air flowrate of 7 L/min**

(a) (b) (c) (d)

**Figure 11. Rising motion of bubbles in the case with plain nozzle for air flowrate with (a) 2 L/min (b) 5 L/min (c) 10 L/min (d) 15 L/min**

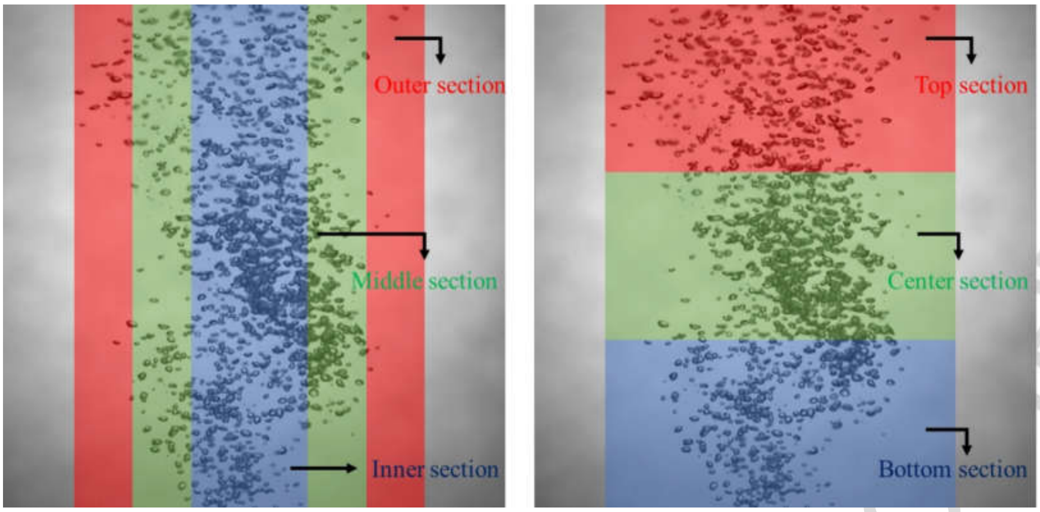


**Figure 12. Radial and axial extraction section for bubble size distribution**

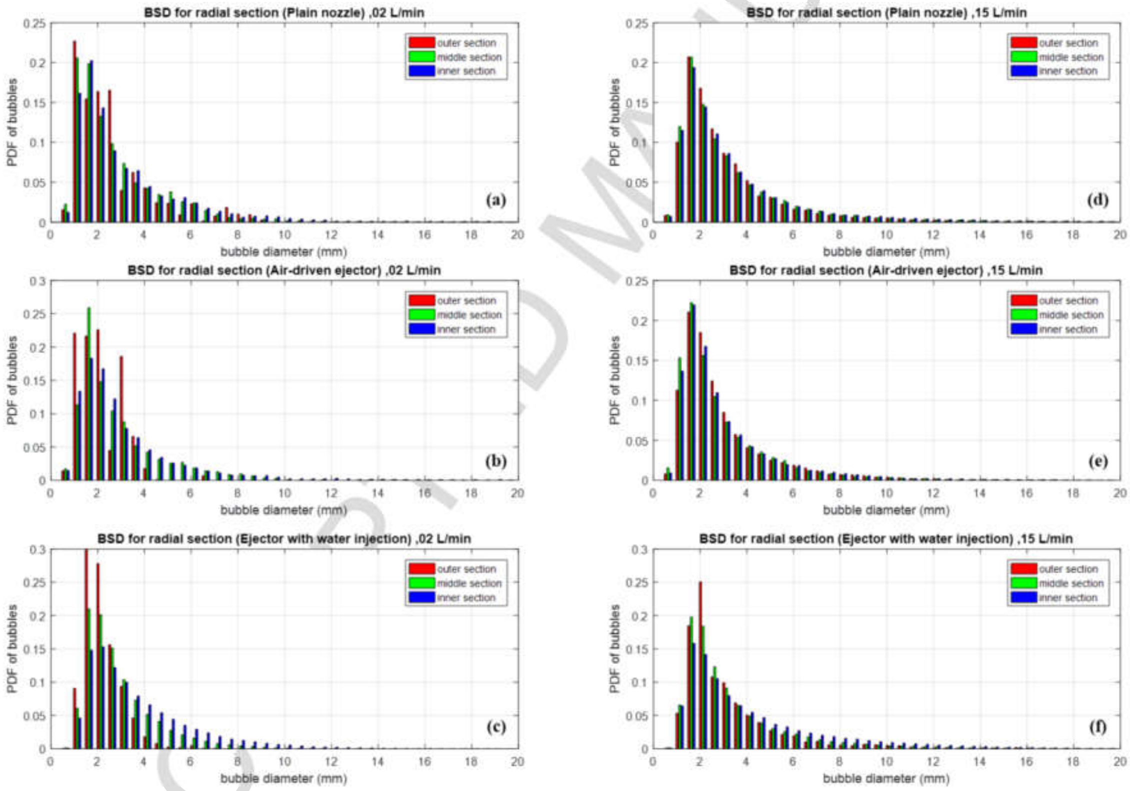


**Figure 13. Radial bubble size distribution for each case.**

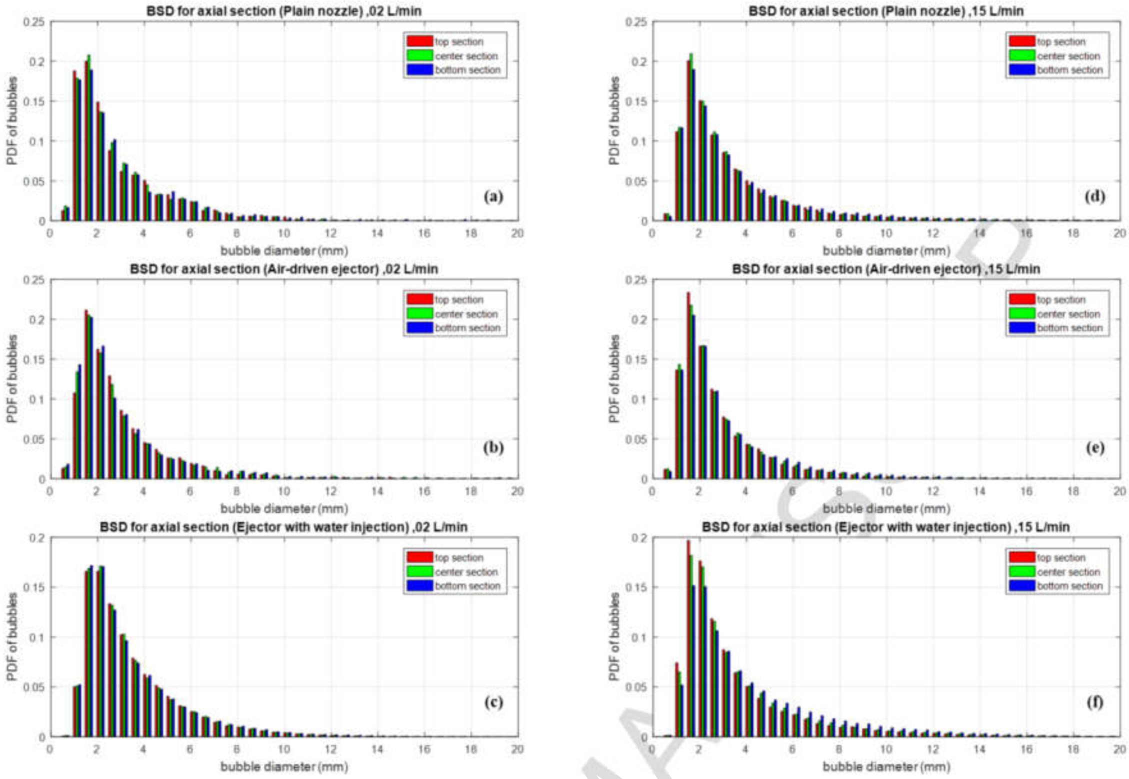


**Figure 14. Axial bubble size distribution for each case**

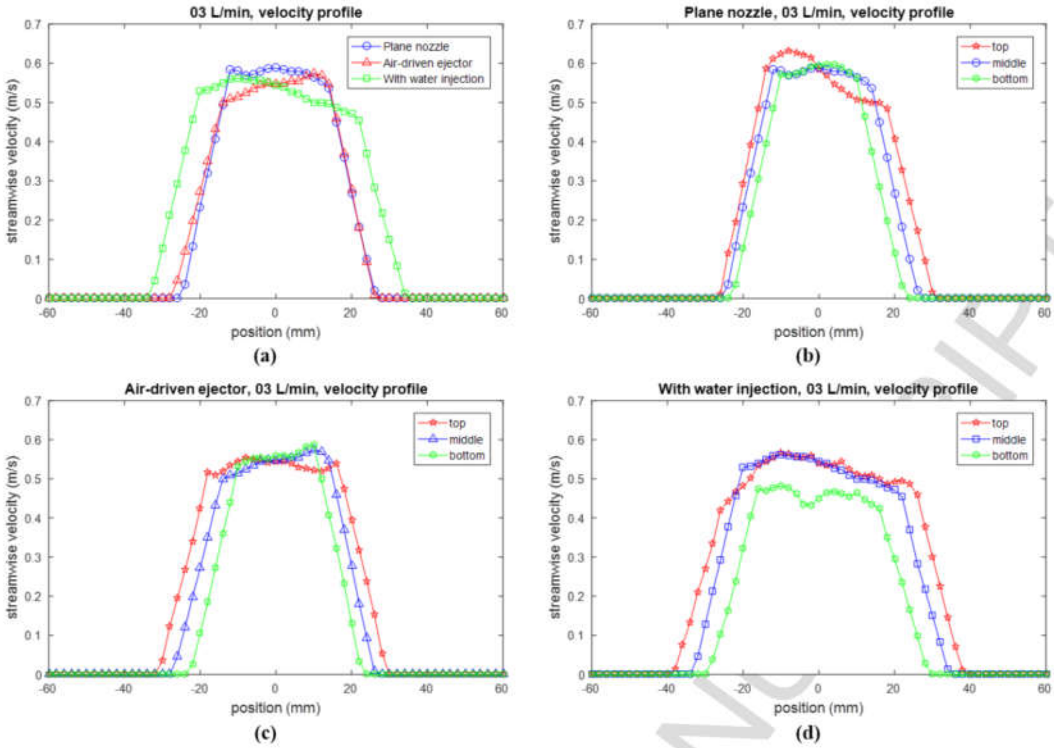


640

641 **Figure 15. Bubble rise velocity profiles: (a) Comparison of each case, (b) Plain nozzle, (c) Air-driven ejector,**
642 **(d) The ejector with water injection case**

643

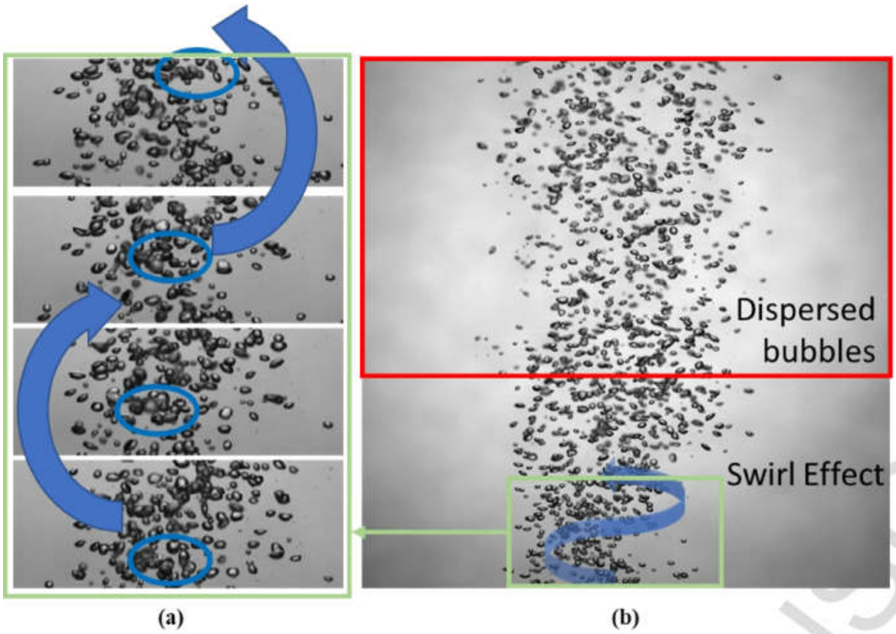


**Figure 16. Bubble generating characteristics of the case with water injection: (a) Sequential motion of bubbles (images of time interval with 40/2000 s), (b) Diminishing of swirl effect in the place far from the ejector**

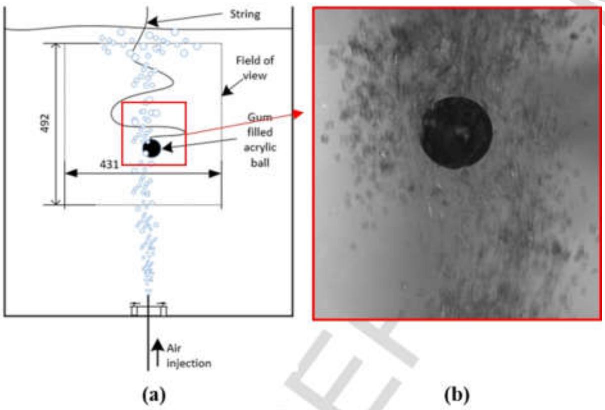


**Figure 17. Schematic of buoyancy experiment: (a) Configuration of experiment setup, (b) Snapshot of the model in bubble swarm of with water injection case**

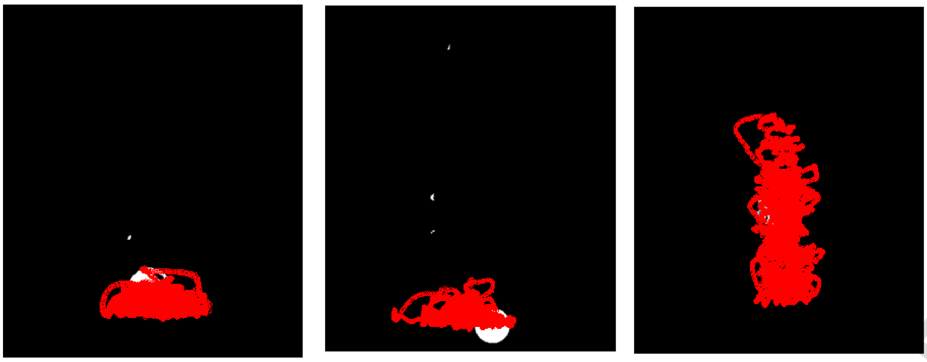

(a) (b) (c)

Figure 18. Sampled trajectory of model during 3000 frames: (a) Plain nozzle, (b) Air-driven ejector, (c) The ejector with water injection

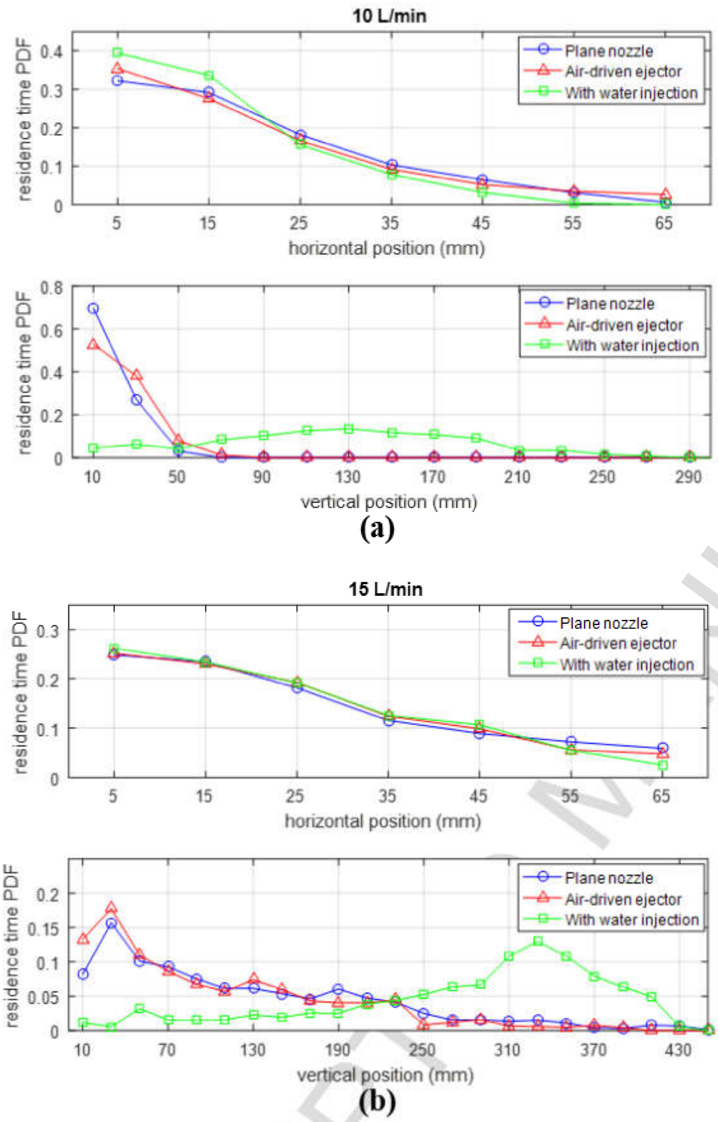


Figure 19. Probability density function of the residence time of the model in each case

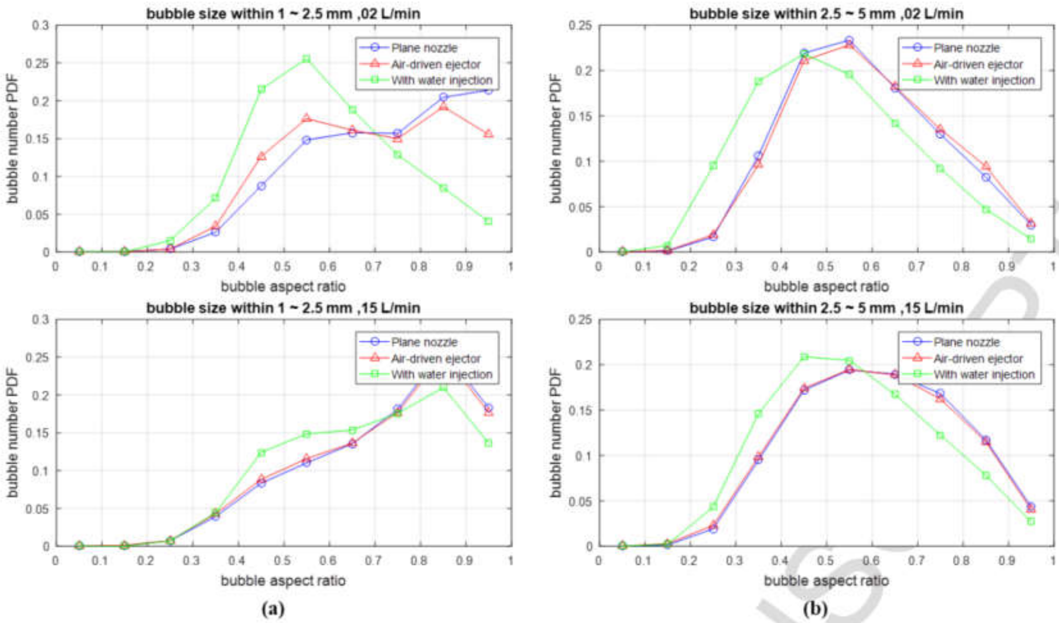


**Figure 20. PDF of bubble aspect ratio with smaller bubbles (a) and larger bubbler (b)**

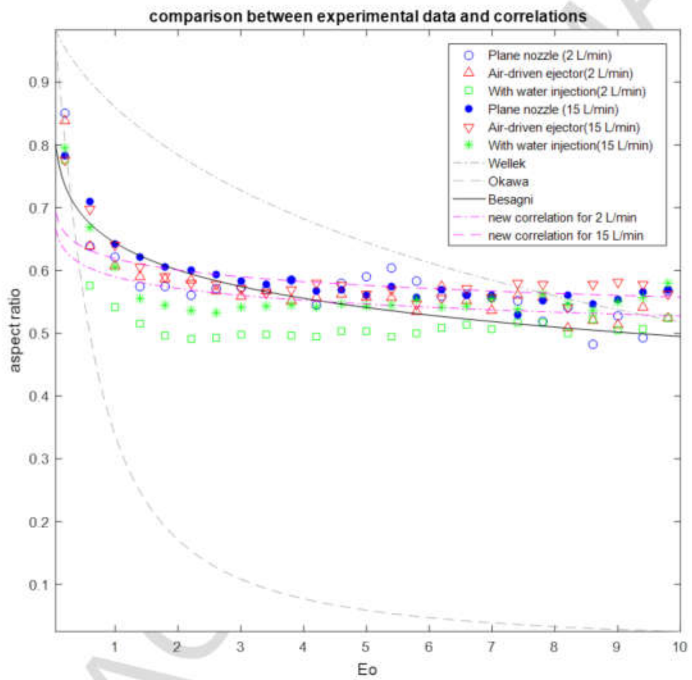


**Figure 21. Bubble aspect ratio from the experimental result and correlations**

**Table 1. Summary on literatures regarding the ejector and the venturi type bubble generator**

| Investigator | experimental conditions and techniques | remarks |
|---|---|---|
| Cramers et al. [10] | Downward ejector in a cylindrical vessel<br>Water flowrate: 2 ~ 7 $m^3/h$<br>Gas-liquid ratio: 0.3 ~ 1.3<br>Measuring concentration of oxygen to measure mass transfer. | In low gas-liquid ratio, increase of gas flow rate cause high IAC (Interfacial Area Concentration) and gas hold-up. |
| Dutta and Raghavan [11] | Downward ejector in a recirculation vessel<br>Water recirculation rate: 0.1 ~ 0.5 $m^3/h$<br>Air entrainment rate: 1.2 ~ 7.5 $m^3/h$<br>Measuring concentration of oxygen to measure mass transfer coefficient | Venturi type ejectors show more effective bubble dispersion performance than other ejectors. |
| Fujiwara et al. [12] | Upward venturi type micro bubble generator with surfactant (3-pentanol) ~ 50ppm<br>Water flowrate: 4.2 ~ 6.7 L/min<br>Bulk void fraction: 2, 4, 20%<br>Measuring transparency to determine purification performance<br>Digital image processing to measure bubble size distribution | PDF of micro bubbles are not affected by the void fraction. It is advantage of this type of bubble generating method in comparison with needle type generator |
| Yin et al. [13] | Venturi type bubble generator with high liquid flowrate but low gas-liquid ratio<br>Water flowrate: 7 ~ 19 $m^3/h$<br>Air volume ratio: 0.1 ~ 0.8% | Develop correlations between nondimensionalized bubble diameter and parameters including We, Re, and other operational conditions. |
| Zheng et al. [14] | Upward ejector with/without swirl body and moderate/low liquid flowrate and gas flowrate.<br>Water flowrate: 0.2 ~ 0.8 $m^3/h$<br>Air flowrate: 0.1 ~ 0.4 $m^3/h$<br>PIV and High-speed photography to measure local bubble size distribution (BSD), gas-liquid interfacial areas, and gas hold-up. | Existence of swirl body occur more energy consumption, larger bubble size, smaller interfacial area, and lower gas hold-up.<br>There were no relationships between BSD and gas fraction. |